

Ring-Substituted α -Arylalanines for Probing Substituent Effects on the Isomerization Reaction Catalyzed by an Aminomutase

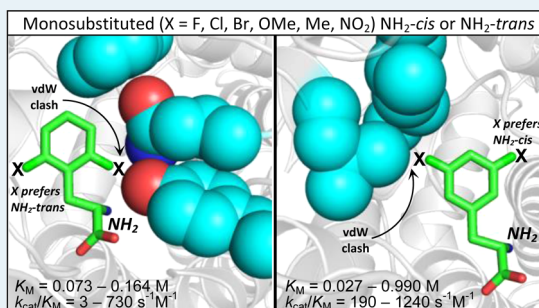
Nishanka Dilini Ratnayake,^{†,||} Nan Liu,^{†,§,||} Leslie A. Kuhn,^{*,§,‡} and Kevin D. Walker^{*,‡,†}

[†]Department of Chemistry, [‡]Department of Biochemistry and Molecular Biology, and [§]Computer Science & Engineering, Michigan State University, East Lansing, Michigan 48824, United States

S Supporting Information

ABSTRACT: β -Amino acids are emerging as an important class of compounds in medicinal chemistry. β -Aryl- β -alanines show antiepileptogenesis activity, while others have been used to synthesize antibiotic β -peptides. To assess the utility of a methylidene imidazolone-dependent *Pantoea agglomerans* phenylalanine aminomutase (*PaPAM*) for making non-natural β -amino acids, we surveyed the substrate specificity of *PaPAM* with several commercially available (*S*)-arylalanine substrates. Here, we report the Michaelis–Menten parameters and catalytic efficiency of *PaPAM* for each substrate. Compared to phenylalanine, substrates containing substituents that were either electron-withdrawing or -donating through resonance or inductive effects affected the k_{cat} of *PaPAM*. Generally, the turnover and catalytic efficiency of *PaPAM* for the *meta*-isomers were better than those for the corresponding *para*- and *ortho*-isomers, with some exceptions. *PaPAM* principally synthesizes the β -amino acids at >90% and the cinnamate byproducts at <10% for 11 of the 19 productive substrates. The yield from other substrates was 14–65% of the cinnamate analogue. Further, to explain the determinants of substrate selectivity of *PaPAM*, a series of substrates with substituents on the aryl ring were docked into the crystal structure of the active site. Induced fit of the protein to accommodate different substituents was modeled computationally by SLIDE docking. The results provide insights into the roles of substrate orientation and conformational flexibility in turnover and indicate which terms of the interaction energy should be accounted for the experimentally observed K_M values, which largely determine catalytic efficiency. Substrate selectivity of *PaPAM* is significantly influenced by steric barriers created by specific active-site residue interactions with the substituted aryl portion of the substrate.

KEYWORDS: aminomutase, MIO, Hammett correlation, kinetics, computational modeling



INTRODUCTION

β -Amino acids are gaining use as building blocks for synthetic β -peptide oligomers that are used as biologically active antibiotics.¹ These β -peptides form ordered secondary structures similar to α -peptides yet are less prone to cleavage than their α -peptide counterparts by most peptidases *in vivo*. In addition, biosynthesizing novel (*S*)- β -amino arylalanines, such as *o*-methyl- β -phenylalanine, has potential application in the synthesis of a pyrazole heterocycle compound that inhibits the function of a lysosomal serine protease cathepsin A (CatA). This inhibition of CatA was shown to prevent the development of salt-induced hypertension.² *m*-Fluoro- β -phenylalanine has also been used as an intermediate in the synthesis of the potent chemokine receptor CCR5 antagonist.³

Enzymatic resolution and catalysis are described as elegant approaches to access enantiopure β -amino acids. Phenylalanine aminomutases from the bacterium *Pantoea agglomerans* (*PaPAM*, EC 5.4.3.11) and an isozyme from *Taxus* plants (*TcPAM*, EC 5.4.3.10) use a 4-methylidene-1*H*-imidazol-5(4*H*)-one (MIO) prosthetic group to isomerize (2*S*)- α -phenylalanine to β -phenylalanine. *TcPAM* makes the (3*R*)- β -amino acid, a precursor of the phenylisoserine side chain on the

pathway to the antimetabolic compound paclitaxel.⁴ In an earlier study, *TcPAM* was shown to convert several variously modified α -arylalanines to their cognate β -isomers.⁵ In contrast, *PaPAM* makes the (3*S*)- β -phenylalanine antipode on the biosynthetic pathway to the antibiotic andrimid (Figure 1).⁶ Knowing the substrate scope of *PaPAM* could increase the range of novel enantiopure β -arylalanines obtained biocatalytically.

Both PAMs belong to a class I lyase-like superfamily of catalysts,^{6–9} along with other MIO-dependent aminomutases. A phenylalanine aminomutase from *Streptomyces maritimus* (*SmpAM*) described earlier as a lyase at physiological conditions was recently characterized as an aminomutase at lower temperatures.⁷ Tyrosine aminomutases (*CcTAM* and *SgTAM*) are used on the biosynthetic pathways to the cytotoxic chondramides in *Chondromyces crocatus*¹⁰ and to the enediyne antitumor antibiotic C-1027, of the neocarzinostatin family, made by *Streptomyces globisporus*.¹¹ A recently characterized aminomutase biosynthesizes (*R*)-2-aza- β -tyrosine from 2-aza- α -

Received: April 9, 2014

Revised: July 23, 2014

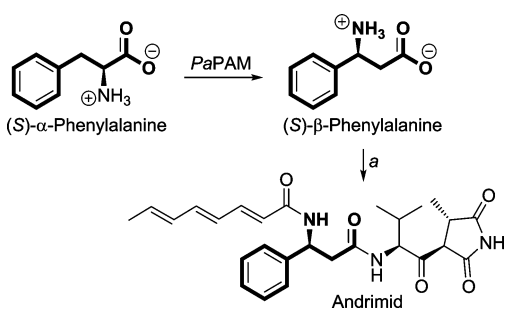


Figure 1. Partial andrimid biosynthetic pathway starting from (*S*)- β -phenylalanine via (*S*)- α -phenylalanine. (a) Several steps.

69 tyrosine found on the biosynthetic pathway to the enediyne
70 kedarcidin in *Streptoalloteichus*.¹²

71 Recent structural characterization of PaPAM supports the
72 formation of an NH₂-MIO adduct, where the amino group of
73 the substrate is covalently attached to the enzyme during α/β -
74 isomerization (Figure 2).¹³ A proton and the NH₂-MIO group

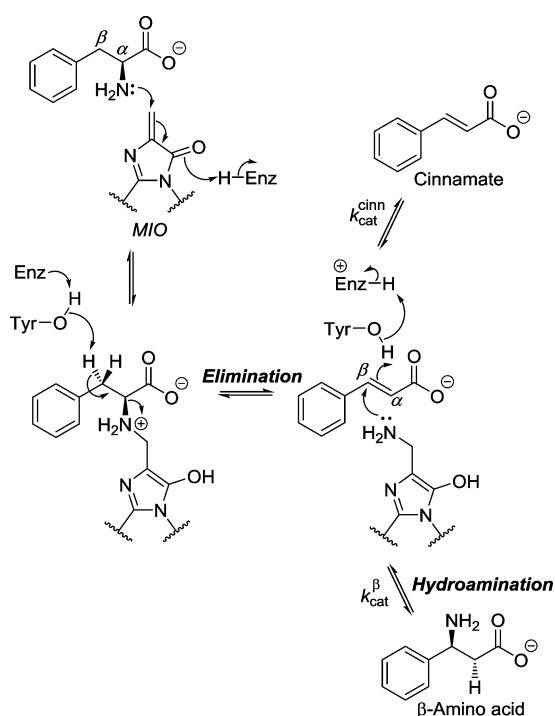


Figure 2. Mechanism of the MIO-dependent isomerization catalyzed by PaPAM. MIO, 4-methylidene-1*H*-imidazol-5(4*H*)-one; $k_{\text{cat}}^{\text{cinn}}$, the rate at which the cinnamate byproduct is released; k_{cat}^{β} , the rate at which the β -amino acid product is released.

75 are eliminated from the substrate to form a cinnamate
76 intermediate (released occasionally as a minor byproduct),
77 followed by hydroamination of the intermediate from NH₂-
78 MIO to form the β -amino acid.

79 The broad substrate specificity of TcPAM encouraged us to
80 investigate, herein, the substrate specificity of the related MIO
81 phenylalanine aminomutase. In addition, structural and
82 mechanistic studies on MIO-based aminomutases are increas-
83 ing our understanding of the reaction chemistry of the enzymes
84 in this family.^{9,13,15–19} Here, to gain further insights on these
85 enzymes, we used computational chemistry to analyze how
86 structural interaction energies relate to the PaPAM isomer-
87 ization kinetics of substrates with different aryl rings. We

propose that PaPAM reaction chemistry is influenced by 88
different properties of the substrate, including sterics, and the 89
magnitude and direction of electronic effects of the substituents 90
on the aryl ring. 91

MATERIALS AND METHODS

Gene Expression and Purification of PaPAM. Luria– 93
Bertani medium (1 L) supplemented with kanamycin (50 $\mu\text{g}/$ 94
mL) was inoculated with 5 mL of an overnight culture of *E. coli* 95
BL21(DE3) cells engineered to express the *papam* cDNA from 96
the pET-24b(+) vector as a C-terminal His₆-tagged PaPAM. 97
These cultures were grown at 37 °C to an optical density of 98
 $A_{600} \sim 0.6$. PaPAM expression was induced with isopropyl- β -D- 99
thiogalactopyranoside (100 μM) at 16 °C, and the cultures 100
were grown for 16 h. The subsequent steps were performed at 101
4 °C, unless indicated otherwise. Cells were harvested by 102
centrifugation at 6,000g (15 min), and the cell pellet was 103
resuspended in lysis buffer (50 mM sodium phosphate buffer 104
containing 5% (v/v) glycerol, 300 mM NaCl, and 10 mM 105
imidazole, pH 8.0). The cells were lysed by sonication (Misonix 106
sonicator, Farmingdale, NY), and the lysate was centrifuged at 107
9,700g (45 min) and then at 102,000g (1 h) to remove cell 108
debris and light membranes. The resultant crude, C-terminal 109
His₆-tagged aminomutase in the soluble fraction was purified by 110
Nickel-nitrilotriacetic acid (Ni-NTA) affinity chromatography 111
according to the protocol described by the manufacturer 112
(Qiagen, Valencia, CA). PaPAM fractions, eluting in 250 mM 113
imidazole, were concentrated by size-selective centrifugal 114
filtration (Centriprep centrifugal filter units, 30,000 MWCO; 115
Millipore), the buffer was exchanged with 50 mM sodium 116
phosphate buffer containing 5% (v/v) glycerol (pH 8.0). The 117
purity of the concentrated enzyme was assessed by SDS–PAGE 118
with Coomassie blue staining, and the quantity was determined 119
by the Bradford protein assay. The overexpressed PaPAM (~59 120
kDa) was obtained at 95% purity (~25 mg/L). 121

Assessing the Substrate Specificity of PaPAM for (2*S*)- 122
 α -Phenylalanine Analogues. (*S*)- α -Phenylalanine and each 123
of its analogues (1 mM) (see Supporting Information) were 124
incubated for 2 h with PaPAM (50 μg) in 1 mL assays of 50 125
mM phosphate buffer (pH 8.0) containing 5% glycerol. Control 126
assays contained all ingredients except that either the substrate 127
or enzyme was omitted. Each reaction was quenched by 128
acidifying to pH 2–3 (6 M HCl). Three internal standards (*m*- 129
fluoro- β -phenylalanine, *p*-methyl- β -phenylalanine, and β -phe- 130
nylalanine at 20 μM) were used, respectively, to quantify three 131
sets of biosynthetic β -amino acids products: set 1, β - 132
phenylalanine; *o*-, *m*-, and *p*-methyl-; *o*-, *m*-, and *p*-methoxy-; 133
m- and *p*-nitro-; *m*- and *p*-chloro- β -phenylalanine; and (2- 134
furyl)- β -alanine; set 2, *o*- and *p*-fluoro; *m*-, and *p*-bromo- β - 135
phenylalanine; and (2-thienyl)- and (3-thienyl)- β -alanine; and 136
set 3, *m*-fluoro- β -phenylalanine (see Supporting Information 137
for β -amino acid resources). Two internal standards (*p*- 138
methylcinnamic acid and cinnamic acid at 20 μM) were used 139
to quantify two sets of biosynthetic aryl acrylic acid products: 140
set 1, cinnamic acid, *o*-, *m*-, and *p*-fluorocinnamic acid, and (2- 141
thienyl)- and (3-thienyl)-acrylic acid; set 2, *o*-, *m*-, and *p*- 142
methyl-; *o*-, *m*-, and *p*-methoxy-; *m*- and *p*-nitro-; *m*- and *p*- 143
chloro-; *m*- and *p*-bromo-cinnamic acid; and (2-furyl)-acrylic 144
acid (see Supporting Information). After acidifying the 145
reactions, the aryl acrylates were extracted with diethyl ether 146
(2 \times 2 mL). The remaining aqueous fractions were basified to 147
pH 10 (6 M NaOH) and treated with ethylchloroformate (50 148
 μL) for 10 min. Each reaction was basified again to pH 10, a 149

150 second batch of ethylchloroformate (50 μL) was added, and
151 each was stirred for 10 min. The solutions were acidified to pH
152 2–3 (6 M HCl) and extracted with diethyl ether ($2 \times 2 \text{ mL}$).
153 For each sample, the diethyl ether fractions were separately
154 combined. The organic fraction was removed under vacuum,
155 and the resulting residue was dissolved in ethyl acetate/
156 methanol (3:1, v/v) (200 μL). The solution was treated with
157 excess (trimethylsilyl)diazomethane until the yellow color
158 persisted. The derivatized aromatic amino acids and aryl
159 acrylates were quantified by GC/EI-MS (see Supporting
160 Information). The peak area was converted to concentration
161 by solving the linear equation obtained from the standard
162 curves constructed with the corresponding authentic standards,
163 quantified by GC/EI-MS (Figures S1–S19 of the Supporting
164 Information).

165 **Kinetic Parameters of PaPAM for (2S)- α -Phenyl-**
166 **alanine Analogues.** PaPAM (10, 25, 50, or 100 $\mu\text{g}/\text{mL}$)
167 was incubated with each productive substrate (1000, 2000, or
168 2250 μM) in 12 mL assays to establish linearity with respect to
169 time at a fixed protein concentration at 31 $^\circ\text{C}$. Aliquots (1 mL)
170 were withdrawn from each assay at 0.5 h intervals over 5 h, and
171 the reactions were quenched by adding 6 M HCl (100 μL).
172 The products were derivatized and quantified as described
173 above, and steady state conditions for each substrate were
174 determined. To calculate the kinetic constants, each substrate
175 was varied (10–2250 μM) in separate assays under the
176 predetermined steady state conditions. Resultant β -aryllalanine
177 and aryl acrylate products were quantified after terminating the
178 reaction as described previously. Kinetic parameters (K_M and
179 $k_{\text{cat}}^{\text{total}}$) were determined from Hanes–Woolf plots by plotting
180 $[S]/v$ against $[S]$ ($R^2 = 0.97$ – 0.99) (Figures 20S–38S of the
181 Supporting Information), where $k_{\text{cat}}^{\text{total}} = (k_{\text{cat}}^{\beta} + k_{\text{cat}}^{\text{cinn}})$; the sum of
182 the production rates of the β -aryllalanine and aryl acrylate,
183 respectively. The latter rates were determined from Hanes–
184 Woolf plots.

185 **Inhibition Assays for Nonproductive Substrates.** (2S)-
186 α -Phenylalanine (at 10, 20, 40, 80, 100, 200, 300, 500, 750, and
187 1000 μM) and PaPAM (10 μg , 0.17 nmol) were mixed and
188 incubated separately for 40 min with nonproductive substrates
189 *o*-chloro-, *o*-bromo-, or *o*-nitro-(S)- α -phenylalanine (at 50, 100,
190 and 200 μM). The products were derivatized and quantified as
191 described earlier. Inhibition constants (K_I) were calculated by
192 nonlinear regression analysis using GraphPad Prism 6 Software
193 (La Jolla, CA).

194 **Modeling Substrate-PaPAM Structural Interactions to**
195 **Understand Selectivity.** To understand the differences in
196 catalytic efficiency, which are largely dictated by differences in
197 K_M , the substrates were modeled in the PaPAM active site.
198 Active configurations of the substrates were generated by
199 overlaying their aryl rings onto the active conformation of α -
200 phenylalanine in the crystal structure by using molecular editing
201 in PyMOL 1.5.0.4 (Schrödinger, Inc., New York, NY) and fixed
202 reference coordinates in OMEGA 2.4.6 (OpenEye Scientific
203 Software).^{14,15} Since the substrates form covalent bonds with
204 binding site residues of PaPAM, their orientation is highly
205 restricted.

206 The position of the *ortho*- or *meta*-substituent breaks the C2
207 axis of symmetry in the phenyl ring of the substrates. Thus, the
208 ring can adopt two configurations that are consistent with the
209 orientation of α -phenylalanine in the crystal structure. In one
210 configuration, called the “ NH_2 -*cis*,” the substituent on the aryl
211 ring is on the same side as the NH_2 group of the phenylalanine
212 substrate. In the other configuration, the “ NH_2 -*trans*,” obtained

by a 180 $^\circ$ rotation about the C_β - C_{ipso} bond, the substituent is 213
oriented on the side opposite the NH_2 group. Alternative low- 214
energy conformations of the substrates, in which the substrate 215
orientation deviated from that of α -phenylalanine in the crystal 216
structure, were sampled using OMEGA 2.4.6 (OpenEye 217
Scientific Software, Santa Fe, NM; <http://www.eyesopen.com>) and analyzed with respect to experimental K_M values. 218
For energy calculations, AM1BCC charges were assigned to the 220
substrates using molcharge 1.3.1 (Open Eye Scientific 221
Software).¹⁶ 222

223 **Calculating Substrate-PaPAM Interaction Energies.** 223
The sum of protein–ligand interaction energy [$E_{(p-l)}$] and 224
ligand internal energy [$E_{(l)}$] values for the 22 substrates was 225
calculated using Szybki^{17–19} 1.7.0 (OpenEye Scientific 226
Software). The electrostatic Coulombic [$E_{C(p-l)}$] and steric 227
van der Waals (vdW) interaction energy [$E_{V(p-l)}$] terms were 228
extracted from the $E_{(p-l)}$ term for each conformer. Steric 229
collisions between the substrates and the binding site residues 230
were visualized pairwise by using a PyMOL script, show_ 231
bumps.py (created by Thomas Holder of Schrödinger, Inc.) 232
showing vdW radius overlaps of 0.1 Å or more. The residues 233
were then grouped according to which overlaps impacted the 234
o-, *m*-, and *p*- positions of substrates. The component energy 235
terms [$E_{(p-l)}$], [$E_{C(p-l)}$], [$E_{V(p-l)}$], and [$E_{(l)}$] were calculated with 236
two protocols to evaluate which approach led to interaction 237
energies that best correlated with the K_M values. First, a single- 238
point energy calculation protocol employing a Poisson– 239
Boltzmann electrostatics model was used when the substrate 240
was placed in the NH_2 -*cis* or NH_2 -*trans* configuration. The 241
 NH_2 -*cis* and NH_2 -*trans* conformers were evaluated without 242
energy minimization. The binding site of the protein was kept 243
in its crystallographic conformation to test the hypothesis that 244
the active complex of the protein and substrate matches the 245
crystallographic conformation observed with α -phenylalanine 246
(PDB entry 3UNV). Second, a two-step protocol recom- 247
mended by the OpenEye Scientific Software was used to 248
explore whether energy minimization could improve the 249
modeling of PaPAM-substrate interactions by reducing any 250
repulsive interactions. The backbone residues of PaPAM were 251
fixed, with the substrates in either the NH_2 -*cis* or NH_2 -*trans* 252
configuration. Protein side chains within 4 Å of the substrates 253
were then allowed to move toward an energy minimum, using 254
the exact Coulomb electrostatics model. Because vdW clashes 255
lead to large, unfavorable interaction energies, this energy 256
minimization protocol reduces vdW overlap by small shifts in 257
active site residues when possible. The energy estimate of each 258
minimized configuration was then refined using the above 259
single-point energy calculation with the Poisson–Boltzmann 260
electrostatics model. 261

262 As an alternative approach, SLIDE (version 3.4) docking^{20,21} 262
was used to model potential conformational changes of the 263
protein and substrate upon binding. SLIDE rotated active site 264
residues to remove or reduce vdW overlap, while the 265
phenylalanine ligands were fixed to maintain their initial 266
 NH_2 -*cis* or NH_2 -*trans* configuration. 267

268 To identify any additional steric or electrostatic factors 268
important for the activity of PaPAM substrates, structure– 269
activity landscape index (SALI) analysis was used to identify 270
“activity cliffs”. These cliffs represent large changes in PaPAM 271
binding affinity among structurally similar substrates.²² For 272
identifying activity cliffs, pairwise comparisons between 273
substrates to measure structural similarity scores were 274
performed using ROCS 2.4.2 software (OpenEye Scientific 275

276 Software).²³ The SALI score was measured as $SALI_{(ij)} = |K_{Mi}$
 277 $- K_{Mj}| / (2 - sim(i,j))$, in which the $sim(i,j)$ value (structural
 278 similarity between molecules i and j) was measured by the
 279 ROCS Tanimoto Combo score (with a maximum value of 2,
 280 reflecting equal contributions from shape and electrostatic
 281 match terms), and K_{Mi} and K_{Mj} were the experimental K_M
 282 values of molecules i and j .

283 ■ RESULTS AND DISCUSSION

284 **Overview of the PaPAM Mechanism.** The PaPAM
 285 reaction goes through a cinnamate intermediate after
 286 elimination of the amino group and benzylic hydrogen from
 287 the α -amino acid substrate. Earlier deuterium isotope studies
 288 ($k_H/k_D > 2$) on a related aminomutase TcPAM suggest the
 289 deprotonation step of the elimination reaction is rate-
 290 determining.²⁴ The coupling between the amine group of the
 291 substrate and the MIO is proposed to make a good alkyl
 292 ammonium leaving group. α,β -Elimination of the β -hydrogen
 293 and α -alkyl ammonium can advance through different routes.
 294 The concerted, one-step E2 (bimolecular elimination)
 295 mechanism proceeds through base-catalyzed removal of an
 296 acidic proton and a leaving group. By comparison, the two-step
 297 E1cB (unimolecular conjugate-base elimination) uses base-
 298 catalysis to remove a proton vicinal to a poor leaving group,
 299 yielding a carbanion intermediate. MIO-dependent amino-
 300 mutase reactions likely follow an E2 or E1cB mechanism, where
 301 both depend on the rate of deprotonation of C_β , as proposed in
 302 an earlier work.²⁵ Thus, electron-withdrawing substituents on
 303 the aryl ring of the substrate that stabilize a δ^- charge on C_β
 304 should therefore increase the rate of the elimination step. In
 305 contrast, the two-step E1 (unimolecular elimination) reaction is
 306 not likely for MIO-dependent reactions. The attached, electron-
 307 withdrawing carboxylate of the substrate would destabilize the
 308 C_α -carbocation formed after displacement of the NH_2 -MIO
 309 adduct (Figure 3A).

310 The final reaction sequence of the MIO-dependent amino-
 311 mutases involves an α,β -addition reaction, where the NH_2 -MIO
 312 and a proton (H^+) add across the double bond of the acrylate
 313 intermediate. To obtain the β -amino acid in a concerted
 314 hydroamination, the polarity of the C_β (δ^+) needs to be
 315 opposite of that in the earlier elimination sequence. Here, the
 316 nucleophilic NH_2 -MIO binds to C_β , and the electrophilic H^+
 317 attaches to C_α (Figure 3B).

318 Alternatively, PaPAM could use a stepwise addition sequence
 319 where the nucleophile (NH_2 -MIO) couples to form a 1,4-
 320 Michael adduct. This conjugate addition route benefits from an
 321 electropositive (δ^+) C_β by delocalizing the π -electrons toward
 322 the carboxylate of the substrate. Theoretically, a substituent that
 323 places negative charge inductively within the ring or mesomeri-
 324 cally on C_{ipso} of the β -aryl acrylate intermediate should also
 325 strengthen the formation of a δ^+ on C_β . These types of
 326 electrostatic considerations, along with binding affinity, were
 327 considered to explain the hydroamination reaction of TcPAM
 328 for aryl acrylate substrates.^{26,27}

329 In earlier accounts, the Michael addition mechanism was
 330 proposed,^{28,29} but a presumed resonance structure has two
 331 repelling oxyanions on the carboxylate of the reactant that
 332 normally forms a monodentate salt bridge (Figure 4a), as
 333 evidenced in the PaPAM crystal structure.¹³ To alleviate
 334 buildup of this electrostatic repulsion, we propose that near-
 335 concerted protonation and amination of the π -bond likely
 336 minimizes the formation of the unfavorable dianion (Figure
 337 4b). A contrasting pathway is envisioned to first add a proton at

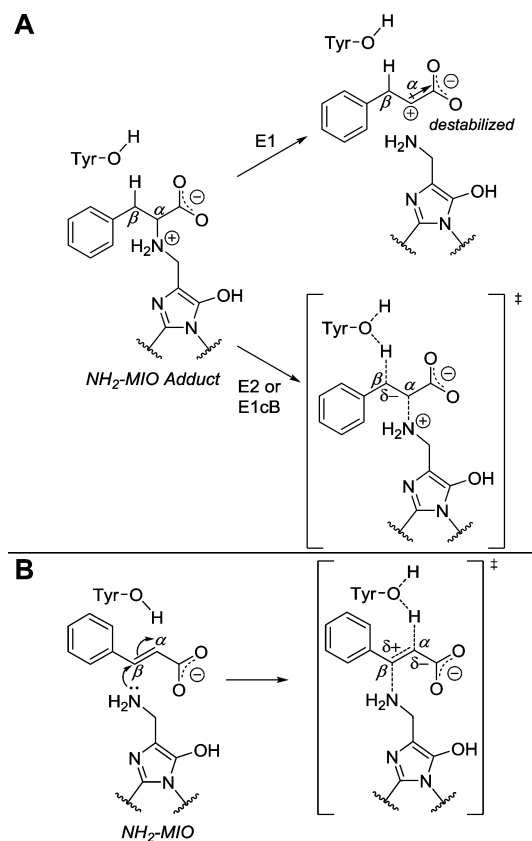


Figure 3. (A) Proposed elimination mechanisms for the displacement of the NH_2 -MIO adduct. E1, unimolecular; E2, bimolecular; and E1cB, conjugate-base eliminations. (B) Concerted hydroamination of the acrylate intermediate. Shown is a transition state intermediate (right) highlighting the polarization of the π -bond in which the nucleophilic NH_2 -MIO and the electrophilic H^+ approach C_β and C_α , respectively.

338 C_α of the acrylate intermediate. The resulting intermediate has
 339 a positive charge (δ^+) on the benzylic C_β , which is resonance
 340 stabilized by the aryl ring and further stabilized by electron-
 341 releasing substituents (Figure 4c). Rapid nucleophilic attack by
 342 the NH_2 -MIO on the carbocation would ensue to complete β -
 343 amino acid catalysis.

344 **Electronic Effects of *ortho*-, *para*-, and *meta*-Sub-**
 345 **stituents.** To gain further insights into the mechanism of
 346 PaPAM, the substrate specificity was queried with 19
 347 phenylalanine analogues and 3 heteroaromatic compounds.
 348 The substituents on the phenyl ring varied in position, size,
 349 inductive and mesomeric effects, polarizability, hydrophobicity,
 350 and the ability to form H- and halogen-bonds. The kinetic
 351 parameters of PaPAM for the natural substrate (**1**) are used to
 352 compare against the values for each analogue (**2–22**).

353 In general, the relative catalytic efficiency (Table 1) for each
 354 analog was negatively affected by a decrease in k_{cat}^{total} and/or
 355 increase in K_M . In addition, the linear correlation coefficient was
 356 calculated between the binding energy and experimental K_M
 357 values for different models of substrate positioning in the
 358 PaPAM binding site. Each substrate was placed in the
 359 crystallographic orientation of the α -phenylalanine substrate,
 360 and the side chains of PaPAM were modeled without energy
 361 minimization in positions guided by the crystal structure. This
 362 crystal structure-like model correlated better with K_M values
 363 than did flexibility modeling of substrate interactions by using
 364 SLIDE or two alternative energy minimization protocols.

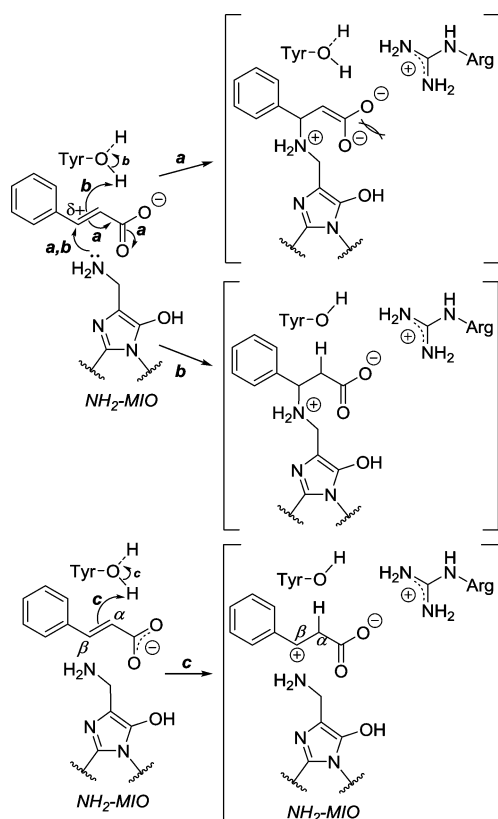


Figure 4. (Route a) A stepwise Michaelis-addition pathway. Shown is an intermediate adduct (top right) with the π -electrons delocalized into the carboxylate group forming a repelling dianion prior to C_{α} -protonation. (Route b) Concerted hydroamination of the acrylate π -bond. Shown is an intermediate (middle right) with maximal charge separation between repelling negative charges in the carboxylate group and the cation and anion. (Route c) A stepwise hydroamination sequence. Shown is a proposed intermediate (bottom right) resulting from C_{α} -protonation as the first step, which places a positive charge at C_{β} . C_{β} is now primed for nucleophilic attack by the NH_2 -MIO adduct.

Table 1. Kinetic Parameters^a of PaPAM for Various Substituted Aryl and Heteroaromatic Substrates

R	K_M	k_{cat}^{β}	k_{cat}^{cinn}	k_{cat}^{total}	k_{cat}^{total}/K_M
1	168 (7)	0.301 92.8%	0.022 7.2%	0.323 (0.013)	1.93 (0.20)
2	339 (15)	0.396 93.9%	0.024 6.1%	0.420 (0.014)	1.24 (0.12)
3	27 (5)	0.027 85.2%	0.004 14.8%	0.031 (0.002)	1.2 (0.4)
4	432 (26)	0.462 95.2%	0.022 4.8%	0.484 (0.02)	1.12 (0.14)
5	29 (1)	0.020 85.7%	0.003 14.3%	0.023 (0.001)	0.79 (0.06)
6	88 (6)	0.055 83.6%	0.009 16.4%	0.064 (0.002)	0.73 (0.09)
7	415 (79)	0.143 34.8%	0.093 65.2%	0.236 (0.01)	0.588 (0.066)
8	337 (27)	0.139 97.2%	0.004 2.8%	0.143 (0.004)	0.428 (0.063)
9	430 (15)	0.136 92.6%	0.01 7.4%	0.146 (0.003)	0.340 (0.025)
10	73 (6)	0.021 95.5%	0.001 4.5%	0.022 (0.001)	0.31 (0.04)
11	990 (124)	0.201 99.0%	0.002 1.0%	0.203 (0.012)	0.209 (0.050)
12	132 (5)	0.024 90.9%	0.002 9.1%	0.026 (0.001)	0.19 (0.02)
13	204 (4)	0.048 78.3%	0.010 21.7%	0.058 (0.001)	0.19 (0.01)
14	491 (82)	0.050 94.1%	0.003 5.9%	0.053 (0.003)	0.11 (0.03)
15	525 (44)	0.043 95.6%	0.002 4.4%	0.045 (0.001)	0.09 (0.01)
16	163 (9)	0.010 63.6%	0.003 36.4%	0.013 (0.001)	0.082 (0.010)
17	752 (39)	0.025 48.0%	0.013 52.0%	0.038 ($<10^{-3}$)	0.050 (0.005)
18	1187 (76)	0.022 97.7%	0.0005 2.3%	0.022 ($<10^{-3}$)	0.019 (0.002)
19	164 (7)	0.002 70.0%	0.0007 30.0%	0.003 ($<10^{-3}$)	0.02 ($<10^{-2}$)
20					
21					
22					

^aStandard errors are in parentheses. Units: s^{-1} for k_{cat} , μM for K_M , and $s^{-1} \cdot M^{-1} \times 10^3$ for k_{cat}^{total}/K_M . Compounds 20–22, not productive.

365 **Substituent Effects on Michaelis Parameters.** *meta*-
 366 **Substituents.** The relative catalytic efficiencies were highest
 367 for *m*-halogenated substrates (2–4) (Table 1). The K_M values
 368 of PaPAM for *m*-bromo (2) and *m*-chloro (4) substrates were
 369 only negatively affected ~ 2 -fold, and the k_{cat}^{total} values remained
 370 essentially unchanged compared to the parameters for 1 (Table
 371 1). Interestingly, the relative k_{cat}^{total} for the *m*-fluoro substrate 3
 372 was ~ 10 -fold lower ($0.031 s^{-1}$) than that for 1, 2, and 4, yet the
 373 5-fold lower K_M of PaPAM for 3 made the k_{cat}^{total}/K_M similar to
 374 those for 1, 2, and 4. The latter suggests that 3 binds tighter
 375 than 2 and 4, which carry halogens (Br and Cl) with larger
 376 atomic radii of 185 and 175 pm, respectively, compared to the
 377 smaller F (147 pm) of 3. In addition, the fluoro group, through
 378 some as yet unknown process, binds better than the natural
 379 substrate containing a smaller H atom.

380 Analysis of other *meta*-substituted substrates showed the
 381 catalytic efficiencies for *m*-nitro (9), *m*-methoxy (11), and *m*-
 382 methyl (13) analogues were 6- to 10-fold lower than that for 1.
 383 The *m*-nitro of 9 only reduced the relative k_{cat}^{total}/K_M of PaPAM
 384 by 5.7-fold due to the modest 2.2- and 2.6-fold negative effects
 385 on k_{cat}^{total} and K_M , respectively, compared with that of 1 (Table
 386 1). To further evaluate the mechanistic basis of the differences
 387 in turnover by PaPAM for various *meta*-substituted substrates,

we gauged the dependence of the relative turnover rate on the 388
 389 substituent of the substrate.

390 The Hammett plot between the calculated $\log(k_{\text{cat}}^{mX}/k_{\text{cat}}^{\text{H}})$ of
 391 *PaPAM* and substituent constants (σ)³⁰ for the *meta*-
 392 substituted (*mX*) arylalanines (*m*-bromo (2), *m*-chloro (4),
 393 *m*-nitro (9), *m*-methoxy (11), and *m*-methyl (13)) follow a
 394 concave-down, parabolic regression curve³¹ (Figure 5A). The

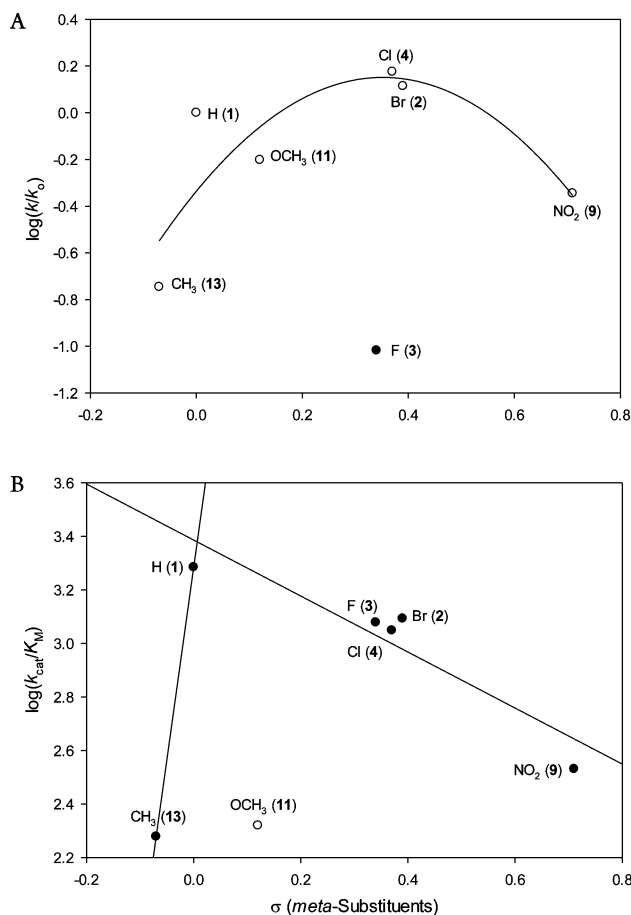


Figure 5. (A) Dependence of the observed $\log(k_{\text{cat}}^{mX}/k_{\text{cat}}^{\text{H}})$ [designated as $\log(k/k_0)$] on the Hammett substituent constant for the *PaPAM*-catalyzed isomerization of *meta*-substituted α -arylalanines. Here, k_{cat}^{mX} is $k_{\text{cat}}^{\text{total}}$ for entries 2–4, 9, 11, and 13; $k_{\text{cat}}^{\text{H}}$ is $k_{\text{cat}}^{\text{total}}$ for entry 1. Correlation coefficient (R) = 0.84. The outlier *m*-fluoro substrate 3 (filled circle) appears at $\log(k/k_0) = -1.02$; $\sigma = 0.06$; $\text{SE}_{\bar{x}} \pm 0.019\text{--}0.033$. (B) Dependence of the observed $\log(k_{\text{cat}}^{mX}/K_{\text{M}})$ [designated as $\log(k_{\text{cat}}/K_{\text{M}})$] on the Hammett substituent constant for the *PaPAM*-catalyzed isomerization of *meta*-substituted α -arylalanines (1–4, 9, 11, and 13). Correlation coefficients: (R) = 0.93 for the linear regression of entries 1 and 13, with a positive-slope ($\rho = 14$). The outlier *m*-methoxy substrate 11 (open circle) appears at $\log(k_{\text{cat}}/K_{\text{M}}) = 2.32$; $\sigma = 0.12$; $\text{SE}_{\bar{x}} \pm 0.024\text{--}0.085$.

395 fastest reactions at the apex of the curve occurred with the *m*-
 396 bromo and *m*-chloro substrates and the slowest with *m*-methyl
 397 and *m*-nitro, at the extremes. The *m*-methoxy substituent
 398 reacted at an intermediate rate.

399 ***m*-Halogens and *m*-Nitro.** Halogens are a group of
 400 substituents of the “push–pull” type. They withdraw electron
 401 density by induction and donate electrons by resonance,
 402 depending on the type of reaction. The overall effect of the
 403 halogens is considered electron-withdrawing as estimated by
 404 their Hammett substituent constants. *m*-Bromo (2) and *m*-
 405 chloro (4) substrates, however, occupy an ambiguous position
 406 at the apex of the Hammett plot (Figure 5A). The right side of

the correlation plot tends toward a slope (ρ) < 0 and suggested
 the rate of the *PaPAM* reaction was slowed by electron-
 withdrawing substituents.

The $\log(k_{\text{cat}}^{mX}/k_{\text{cat}}^{\text{H}})$ for *m*-nitro substrate 9 fits on the negative
 slope ($\rho \approx -1.4$) of the correlation curve (Figure 5A). The
 strong electron-withdrawing *m*-nitro group is foreseen to
 accelerate deprotonation of C_β that produces a transient δ^-
 on the elimination step (Figure 6A). In turn, the nitro group

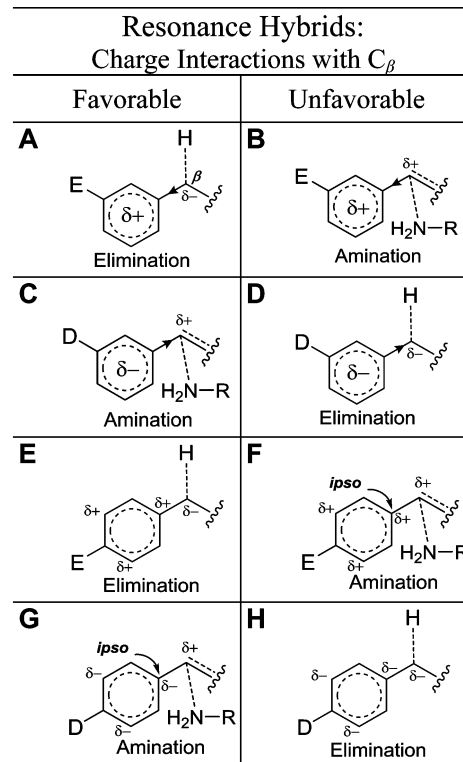


Figure 6. Resonance hybrids formed from electron-donating (D) or -withdrawing (E) substituents on the phenyl ring. An increase or decrease in electron density, caused by the substituent, within the ring or at C_{ipso} is predicted to support a transient δ^+ or δ^- , respectively, at C_β . Resonance hybrids that support an electronegative (δ^-) C_β are proposed to increase the rate of initial elimination, while those that support an electropositive (δ^+) C_β are viewed to increase the hydroamination rate.

was anticipated to affect the β -amination step, which forms a
 transient δ^+ on C_β (Figure 6B). The resonance hybrid of the *m*-
 nitro group places δ^+ on carbons flanking, but not directly on,
 C_{ipso} . The *m*-nitro group was therefore expected to slow the
 amination rate of the *PaPAM* reaction involving 9 compared to
 that for 1. The *m*-nitrocinnamate (7.4%)/*m*-nitro- β -amino acid
 product ratio apportioned similar to that of analogous
 products made from 1. This result suggested that the *m*-nitro of
 9 likely had a less than imagined effect on the hydroamination
 of the *m*-nitrocinnamate intermediate. Thus, the intermediate
 was still released as a byproduct presumably at a slower rate
 than the rate of hydroamination.

In contrast, substrates 2 and 4 were turned over ~ 3 -fold
 faster than 9 (Table 1). The “push–pull” effect of 2 and 4 likely
 tells that electron-release by *m*-bromo and *m*-chloro reduces the
 electron-withdrawing magnitude that negatively affects the rate,
 as did the *m*-nitro of 9. The balanced electron-withdrawing
 effect of bromo and chloro likely support the transient δ^- on C_β
 and increases the rate of the elimination step (Figure 6A); the

434 electron-donating effect would improve stabilization of a
435 transient δ^+ formed during the hydroamination across the
436 double bond of the intermediate (Figure 6C).

437 It is worth noting that the proportions of *m*-halo- β -amino
438 acids (93.9% *m*-bromo- β -amino acid and 95.2% *m*-chloro- β -
439 amino acid) and *m*-halo-cinnamate (6.1% *m*-bromo-cinnamate
440 and 4.8% *m*-chloro-cinnamate) made by *PaPAM* from **2** and **4**,
441 respectively, were similar to that of analogous products made
442 from **1** (Table 1). Thus, the amination of the *m*-halocinnamate
443 intermediates was likely not significantly affected by the
444 substituents. This observation supports a mechanism where
445 release of the intermediate as a byproduct is slower than
446 hydroamination.

447 Interestingly, based on Hammett constants, the inductive
448 effects of the fluoro group ($\sigma = 0.34$) on an aryl ring are in
449 principle similar to those of the chloro- ($\sigma = 0.37$) and bromo-
450 ($\sigma = 0.39$) substituents.³⁰ Therefore, it was surprising that the
451 *m*-fluoro substrate **3** had a significantly lower $\log(k_{\text{cat}}^{mX}/k_{\text{cat}}^H)$
452 value and did not fit the Hammett correlation for the *meta*-
453 substituent series (Figure 5A). The significant decrease (~ 10 -
454 fold) in $k_{\text{cat}}^{\text{cinn}}$ and k_{cat}^{β} of *PaPAM* for **3** (compared with the same
455 parameters for **1**) suggested that the *m*-fluoro substituent
456 affected the chemistry at C_{β} during the elimination and the
457 hydroamination steps. The higher proportion of *m*-fluorocin-
458 namate (14.8%) relative to *m*-fluoro β -amino acid (85.2%)
459 made by *PaPAM* from **3**, (compared with the cinnamate
460 (7.2%) and β -amino acid (92.8%) products made from **1**)
461 suggested that the electronic effects of the *m*-fluoro compound
462 affected the amination step more than the elimination step.

463 *m*-Methoxy and *m*-Methyl Substrates. *m*-Methoxy and *m*-
464 methyl substrates **11** and **13**, respectively, appear on the
465 Hammett correlation plot where the slope (ρ) $\approx +2.9$ (Figure
466 5A). This suggested that the *PaPAM* rate was markedly slowed
467 by stronger electron-donating *meta*-substituents. The larger 9.3-
468 fold decrease in the relative $k_{\text{cat}}^{\text{total}}/K_M$ for **11** was principally
469 influenced by the 5.9-fold increase in K_M compared with that
470 for **1**. The increased K_M suggested that the sterics of the *m*-
471 methoxy substrate affected substrate binding. However, the $k_{\text{cat}}^{\text{total}}$
472 for **11** was only 1.6-fold lower than that for **1** and correlated
473 well with the Hammett constants for *meta*-substituents (Figure
474 5A).

475 On the basis of the Hammett constant (+0.12),³⁰ *m*-methoxy
476 has an electron-withdrawing component that slightly reduces
477 the significant *meta*-substituent effect of its electron-donation
478 into the ring by resonance. The *m*-methoxy substituent likely
479 destabilizes the δ^- on C_{β} upon removal of H_{β} (Figure 6D) and
480 decreases the elimination rate. Reciprocally, electron-donation
481 by the *m*-methoxy substituent would promote formation of an
482 electrophilic (δ^+) C_{β} (Figure 6C) formed during the amination
483 step. Here, the electronic effects of the *m*-methoxy that
484 deterred the elimination rate were likely offset by the rate-
485 enhancing effects on the amination step.

486 An earlier study showed that *PaPAM* catalyzes the α/β -
487 isomerization of phenylalanine entirely intramolecularly. The
488 results of the earlier work told that the aminomutase tightly
489 holds the cinnamate intermediate, thus preventing it from
490 exchanging with exogenous cinnamate added at high
491 concentration.²⁹ In the current study, the *PaPAM*-catalyzed
492 product pool from **11** contained the *m*-methoxy- β -amino acid
493 (99.0%) and the *m*-methoxy acrylate at 1.0%. *PaPAM*
494 converted **1** with less selectivity (β -isomer at 92.8%; cinnamate
495 at 7.2%). This supported that the amination efficiency to make
496 the β -isomer of **11** was most likely facilitated by the substituent.

A methyl-substituent contributes electron density through
hyperconjugation (quasi-mesomeric)³² to the attached aryl ring
and exerts resonance effects, to a lesser extent, but similar to
those of methoxy.³⁰ The $\log(k_{\text{cat}}^{mX}/k_{\text{cat}}^H)$ for **13** with an electron-
“releasing” *m*-methyl ($\sigma = -0.07$) fits on the parabolic
Hammett correlation curve (Figure 5A). The steep slope in
this region suggested that the rate of the *PaPAM* reaction is
strongly affected by the electron-releasing *meta*-substituent.
Despite the smaller *meta*-substituent constant for methyl than
for methoxy, the mesomeric *m*-methoxy releases more electron
density to the ring than the methyl does through hyper-
conjugation. We therefore postulated that the rate enhance-
ment of the addition step, through a favorable transition state
(Figure 6C), with **13** was not as significant as with **11**. This
likely accounted for the >3.5 -fold faster $k_{\text{cat}}^{\text{total}}$ for *m*-methoxy **11**
than for *m*-methyl substrate **13**.

The product pool catalyzed by *PaPAM* from **13** contained
more cinnamate analogue (21.7%) compared to that made
from other *m*-substituted substrates **2**, **4**, **9**, and **11** that
contained between 1.0% and 7.4%. We propose that the
amination of the *m*-methyl aryl acrylate is more sensitive to the
effects of the substituent. *m*-Fluoro substrate **3** was converted
to the cinnamate analogue (14.8%) at a similar proportion as
was **13**. Compared with **1**, it is intriguing that substrates **3** and
13, with opposing electronic and steric properties, similarly
affect the k_{cat} of *PaPAM* and the ratio of the cinnamate/ β -
amino acid analogues.

The K_M of *PaPAM* for *m*-methyl substrate **13** was only
slightly affected (1.2-fold) for the less sterically demanding
methyl, compared to the methoxy group of **11**. However, the
 $k_{\text{cat}}^{\text{total}}$ for **13** was surprisingly 5.6-fold slower than that for **1** and
nearly 4-fold slower for **11**. To help explain these observations,
we look at the lone pair geometry predicted by earlier *ab initio*
calculations of an isolated alcohol molecule.³³ This earlier work
predicted the angle between geminal electron pairs of the
oxygen atom was greater than the typical 109.5° between sp^3 -
hybrid orbitals. Using this principle, the methoxy group of **11**
can likely place the less steric lone pairs of electrons and methyl
group on the central oxygen atom in a favorable conformation
so the substrate remains catalytically competent. By contrast,
the methyl substituent of **13** has three overlapping sp^3 -s orbitals
forming the C–H bonds. Even though the methyl group of **13**
is sterically smaller than the methoxy group of **11**, the
tetrahedral geometry of the methyl hydrogens may cause **13** to
adopt a potentially undesirable orientation for catalysis. These
considerations for the *m*-methyl and *m*-methoxy groups are
further supported by findings from the computational analyses,
described later herein.

meta-Substituent Effects on Catalytic Efficiency. The plot
between $\log(k_{\text{cat}}^{mX}/K_M)$ and σ for the *meta*-substituted (*mX*)
arylanilines (Figure 5B) showed that the substituent effects on
the catalytic efficiency (k_{cat}^{mX}/K_M) largely paralleled the nonlinear
relationship between $\log(k_{\text{cat}}^{mX}/k_{\text{cat}}^H)$ and σ (Figure 5A). That is,
the catalytic efficiency decreased paradoxically with substituents
of higher electron-withdrawing or -donating strength. Thus, the
substituent effects on the k_{cat} value of the catalytic efficiency
were not masked by the K_M . Interestingly, the *m*-fluoro (**3**)
substrate fit the linear regression of the plot between $\log(k_{\text{cat}}^{mX}/K_M)$
and σ ($\rho = -1.05$). The effects of the electron-withdrawing
m-fluoro substituent on the catalytic efficiency correlated well
with those of *m*-chloro and *m*-bromo (Figure 5B). Substrate
3 was an outlier, however, on the parabolic regression plot of
 $\log(k_{\text{cat}}^{mX}/k_{\text{cat}}^H)$ and σ (Figure 5A). Reciprocally, the *m*-methoxy

560 (11) substrate fit the parabolic regression of the plot between
 561 $\log(k_{\text{cat}}^{\text{mX}}/k_{\text{cat}}^{\text{H}})$ and σ (Figure 5A), and was an outlier on the
 562 $\log(k_{\text{cat}}^{\text{mX}}/K_{\text{M}})$ correlation plot (Figure 5B). This result suggested
 563 that the catalytic efficiency of PaPAM for substrates 3 and 11
 564 was influenced more by their affinity for PaPAM than by
 565 electronic substituent effects. The relatively low K_{M} (27 μM)
 566 for 3 likely revealed that the acrylate intermediate and β -amino
 567 acid products were also released poorly and affected the
 568 turnover. In contrast, the high K_{M} (990 μM) for 11 suggested
 569 poor substrate binding, which masked the correlation between
 570 the electronic effects of the *m*-methoxy group and catalytic
 571 efficiency.

572 *para*-Substituents. Each substrate containing a *para*-
 573 substituent (5, 14–18), however, significantly reduced the
 574 $k_{\text{cat}}^{\text{total}}$ of PaPAM by 6–25-fold compared to the value for 1 ($k_{\text{cat}}^{\text{total}}$
 575 = 0.323 s^{-1}). As seen for the trend with the *meta*-substituent
 576 series, the *p*-bromo and *p*-chloro substrates were turned over
 577 the fastest; the chloro substrate was turned over slightly faster.
 578 The substrates turned over the slowest by PaPAM in this series
 579 contained a *p*-nitro, *p*-methyl, or *p*-methoxy (Table 1). The
 580 calculated $\log(k_{\text{cat}}^{\text{mX}}/k_{\text{cat}}^{\text{H}})$ of PaPAM and substituent constants
 581 (σ) for the *para*-substituted arylalanines (*p*-fluoro (5), *p*-chloro
 582 (14), *p*-bromo (15), *p*-methyl (16), *p*-nitro (17), and *p*-
 583 methoxy (18)) do not follow a single Hammett plot (Figure
 584 7A). By analogy, the parabolic concave-down Hammett plot for
 585 the *meta*-substituted substrates showed a gradual change in the
 586 reaction step on the PaPAM pathway that was sensitive to the
 587 *meta*-substituent. Likewise, for the *para*-substituents, the
 588 intersecting linear regressions of the opposite slope (ρ) (Figure
 589 7A) suggest the substituent effects transition from affecting the
 590 elimination step to affecting the amination step.³¹

591 The resonance hybrid of the *p*-nitro substrate 17 has a δ^+
 592 directly on C_{ipso} attached to C_{β} (Figure 6E). While this was
 593 imagined to strongly increase the elimination rate (i.e.,
 594 facilitates H_{β} proton removal), the 8.5-fold slower $k_{\text{cat}}^{\text{total}}$ of
 595 PaPAM for 17 (0.031 s^{-1}) than that for 1 (Table 1) likely
 596 resulted because the *p*-nitro slowed the hydroamination rate
 597 (i.e., deterred nucleophilic attack at C_{β}) (Figure 6F) more than
 598 it improved the elimination rate. The higher ratio of *p*-
 599 nitrocinnamate (52%) compared to cinnamate (7.2%) made
 600 from 1 further supports an affected hydroamination step.

601 The effects of the electron-withdrawing *p*-chloro and *p*-
 602 bromo of substrates 14 and 15 on C_{ipso} are lower than those for
 603 the corresponding *meta*-isomers. The lone-pair electrons of the
 604 former, however, can delocalize by resonance and place a δ^-
 605 directly on C_{ipso} attached to C_{β} in the resonance hybrid. The δ^-
 606 will promote the amination step (Figure 6G), yet dramatically
 607 retard the deprotonation of the elimination step of the PaPAM
 608 reaction (Figure 6H). Likewise, the electron-releasing *p*-methyl
 609 of 16 and *p*-methoxy of 18 also place a δ^- on C_{ipso} of the
 610 substrate via hyperconjugation and resonance, respectively.
 611 Each theoretically causes the $\text{p}K_{\text{a}}$ of H_{β} to increase and
 612 discourages the deprotonation of the presumed rate-limiting
 613 elimination step. The Hammett constituent constants predicted
 614 the electron-releasing *p*-methyl substituent would affect
 615 PaPAM turnover ($k_{\text{cat}}^{\text{total}} = 0.013 \text{ s}^{-1}$) more than the methoxy
 616 group, as observed (Figure 7A and Table 1). PaPAM has a ρ
 617 value (+4.74) much greater than unity for the electron-
 618 donating substrates 16 and 18, suggesting that catalysis is very
 619 dependent on the nature of these substituents. By comparison,
 620 the $\rho \approx -1.0$ for substrates 14, 15, and 17 suggests a moderate
 621 yet significant dependence on the electron-withdrawing
 622 strength of the substituent (Figure 7A).

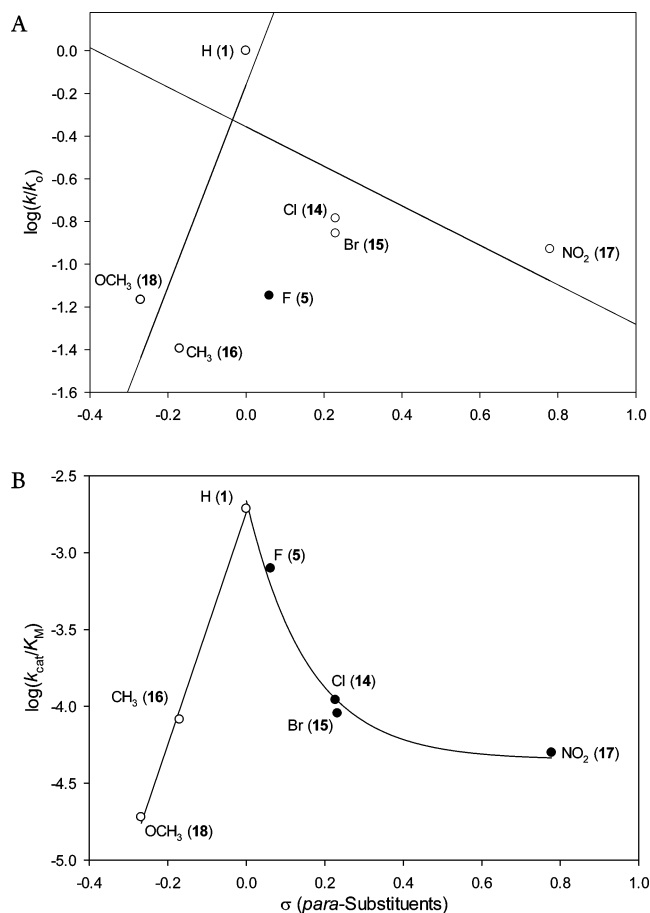


Figure 7. (A) Dependence of the observed $\log(k_{\text{cat}}^{\text{mX}}/k_{\text{cat}}^{\text{H}})$ [designated as $\log(k/k_0)$] on the Hammett substituent constant for the PaPAM-catalyzed isomerization of *para*-substituted α -arylalanines. Here, $k_{\text{cat}}^{\text{mX}}$ is $k_{\text{cat}}^{\text{total}}$ for entries 14, 15, 16, 17, and 18; $k_{\text{cat}}^{\text{H}}$ is $k_{\text{cat}}^{\text{total}}$ for entry 1. The outlier *p*-fluoro substrate 5 (filled circle) appears at $\log(k/k_0) = -1.15$; $\sigma = 0.06$. Correlation coefficients: (R) = 0.87 for the positive-slope and ($\rho = +4.74$) for the linear regression of entries 1, 16, and 18; (R) = 0.71 for the negative-slope and ($\rho = -0.93$) for the linear regression of entries 1, 14, 15, and 17; $\text{SE}_{\bar{x}} \pm 0.018$ –0.038. (B) Dependence of the observed $\log(k_{\text{cat}}^{\text{mX}}/K_{\text{M}})$ [designated as $\log(k_{\text{cat}}/K_{\text{M}})$] on the Hammett substituent constant for the PaPAM-catalyzed isomerization of *para*-substituted α -arylalanines. Here, k_{cat} is $k_{\text{cat}}^{\text{total}}$ for entries 5, 14, 15, 16, 17, and 18. Correlation coefficients: (R) = 0.99 for the decay curve for entries 1, 5, 14, 15, and 17; (R) = 1.0 for the linear regression of entries 1, 16, and 18 with a positive-slope ($\rho = 7.50$); $\text{SE}_{\bar{x}} \pm 0.024$ –0.076.

In addition, the binding affinity of PaPAM for 16 ($K_{\text{M}} = 163$ μM) and the natural substrate 1 ($K_{\text{M}} = 168$ μM) was similar, 624 while the $k_{\text{cat}}^{\text{total}}$ for 16 was 25-times slower than for 1, further 625 suggesting a strong sensitivity of the reaction rate to the *p*- 626 methyl group (Table 1). Taken together, these results suggest 627 that the magnitude and direction of the electron-releasing or 628 -withdrawing effect of the *para*-substituents affect the isomer- 629 ization rate. That is, electron-releasing substituents affect the 630 deprotonation step of the elimination reaction, while the 631 electron-withdrawing groups affect the nucleophilic addition 632 step catalyzed by PaPAM. 633

The *p*-fluoro substrate 5 was turned over by PaPAM at about 634 the same rate as the *m*-fluoro substrate 3, but coincidentally at 635 the same rate as the other *para*-substituted substrates. It seems 636 that regardless of regiochemistry, the overarching electronic 637 effect(s) of the fluoro substituent stalls the elimination and 638

639 hydroamination steps. In addition, based on the β -amino acid/
640 aryl acrylate (85.7:14.3) distribution catalyzed by PaPAM from
641 **5**, it seems that the fluoro group affects the efficiency of the β -
642 amination step compared to the reaction involving **1**. A similar
643 product distribution was seen herein for the *m*-fluoro substrate
644 **3**.

645 *para*-Substituent Effects on Catalytic Efficiency. The
646 relationship between $\log(k_{\text{cat}}^{pX}/K_M)$ and σ for the *para*-
647 substituted (*pX*) arylalanines (Figure 7B) showed a similar
648 trend in substituent effects on the catalytic efficiency (k_{cat}^{pX}/K_M)
649 as seen between $\log(k_{\text{cat}}^{pX}/k_{\text{cat}}^H)$ for PaPAM and Hammett
650 substituent constants (Figure 7A). There was a strong,
651 nonlinear correlation between decreasing catalytic efficiency
652 and strongly electron-withdrawing and -donating substituents.
653 As with the *meta*-substituents, the catalytic efficiency of PaPAM
654 was also sensitive to the *para*-substituents. Intriguingly,
655 linear dependency of the catalytic efficiency on the *para*-
656 substituent reduced as a combination of electron-withdrawing
657 or -donating strength and increasing K_M for the substrate
658 (Figure 7B and Table 1). This informed us that a reduction in
659 catalytic efficiency was principally dictated by large K_M and not
660 by the electronic effects of the *para*-substituent that separately
661 affected k_{cat} (Figure 7A).

662 *ortho*-Substituents. Interestingly, the K_M values of PaPAM
663 for each of the three productive *ortho*-substrates (**6**, **10**, and **19**)
664 varied only between 1- and 2-fold compared to that of **1**.
665 Seemingly, the *ortho*-substituents, regardless of size, including
666 the bulkier *o*-methoxy of **19**, did not affect substrate binding. Of
667 the three, PaPAM turned over the *o*-methyl substrate (**6**) faster
668 (0.064 s^{-1}) than the *o*-fluoro (**10**, 0.022 s^{-1}) and *o*-methoxy
669 (**19**, 0.003 s^{-1}) compounds (Table 1). However, each was
670 isomerized substantially slower (5-, 14-, and 108-fold,
671 respectively) than **1**. Similar to the *para*-substituents, *ortho*-
672 substituents exert strong resonance and moderate inductive
673 electronic effects that influence the chemistry at certain carbons
674 of an aryl ring (see Figure 6). We propose that electron-
675 donating *ortho*-substituents (methyl, halogens, and methoxy)
676 placed δ^- on C_{ipso} of the substrates. The relatively satisfactory
677 binding (i.e., low K_M values) yet poor turnover for **6**, **10**, and **19**
678 suggests either that PaPAM binds these substrates in a
679 catalytically ineffective orientation or that their electron-donor
680 substituents slow the deprotonation step of catalysis. It should
681 be noted that the *ortho*-substituents on the arylalanine
682 substrates are positioned vicinally to the alanine side chain.
683 The proximity of these groups to the alanyl side chain of the
684 substrates likely creates a steric barrier that skews the aryl ring
685 plane. A canted aryl ring would relax the sterics yet reduce
686 potentially beneficial resonance effects of the substituents on C_β
687 in a charged transition state that could influence substrate
688 turnover.

689 We expected the *o*-bromo, *o*-chloro, and *o*-nitro substrates
690 **20–22** to have productive kinetics similar to those of the
691 corresponding *para*-isomers since *ortho/para*-substituents of
692 the same type exert similar electronic effects (Figure 6A and C).
693 Interestingly, **20–22** did not yield any detectable product in the
694 enzyme reaction. However, their competitive inhibition
695 constants (K_I) of $15.9 (\pm 1.67)$, $17.7 (\pm 2.11)$, and 16.9
696 (± 3.35) μM indicate that they bind well to PaPAM. The lack of
697 turnover of **20–22** by PaPAM was therefore likely caused by
698 poor access of the substrates to a catalytically competent
699 conformation.

700 *Heteroaromatic Substrates*. After understanding the *ortho*-,
701 *para*-, and *meta*-directing character of the substituents, the

influence of heteroatoms on the distribution of electron density 702
in resonance structures of the aromatic ring was not difficult to 703
predict. Evaluation of a resonance hybrid of 3-thienylalanine 704
(**8**) showed that a δ^- charge resides on C_{ipso} of the thienyl ring 705
(Figure 8A, resonance path a). We noted an analogous δ^- 706

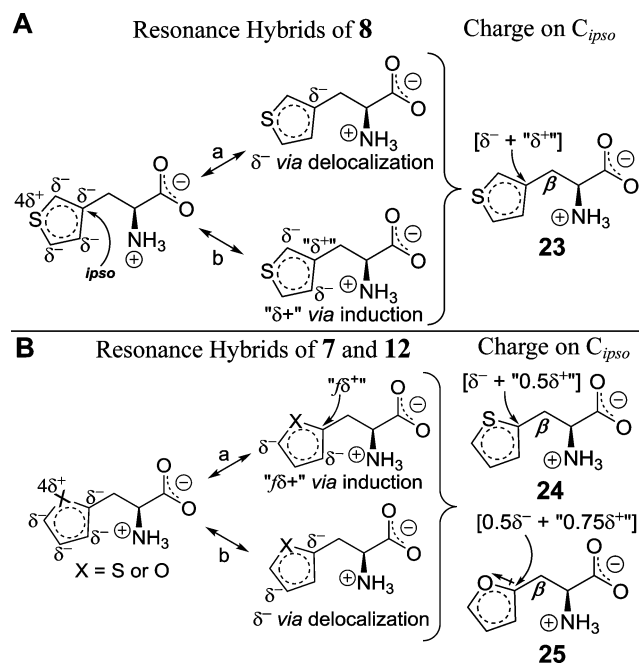


Figure 8. (A) Resonance hybrids of 3-thienylalanine (**8**) and (B) composite resonance hybrids of 2-furylalanine (**7**) and 2-thienylalanine (**12**); a dipole moment is illustrated. Also shown are the partial (δ) charges resulting from a combination of the charges present in the canonical structures obtained through delocalization of electrons in the extended aromatic π -system. The induced charges on C_{ipso} are designated in quotation marks. Charges are weighted arbitrarily by fractional numbers (f) to illustrate their relative contribution at C_{ipso} in **23**, **24**, and **25**.

charge on C_{ipso} of productive substrates (**5**, **14–18**) containing 707
an electron-donating *para*-substituent on the phenyl ring (see 708
Figure 6G or H). We proposed that this electronic effect 709
slowed the deprotonation of the presumed rate-limiting 710
elimination step. For substrate **8**, however, the vicinal δ^- 711
charges induce a δ^+ on the C_{ipso} , which is imagined to reduce 712
the magnitude of the δ^- at C_{ipso} (Figure 8A, resonance path b). 713
Thus, the lower magnitude δ^- at C_{ipso} of **8**, compared to the δ^- 714
at C_{ipso} for **5** and **14–18** ($0.013–0.053 \text{ s}^{-1}$), likely affected the 715
rate-determining deprotonation step less, as evidenced by its 3- 716
to 10-fold higher $k_{\text{cat}}^{\text{total}}$ of PaPAM for **8** (0.143 s^{-1}). 717

The effect of a reduced δ^- at C_{ipso} of **8** likely also explains 718
why PaPAM catalyzed **8** \sim 6-fold faster than 2-thienylalanine 719
(**12**, 0.026 s^{-1}). One resonance hybrid of **12** has one δ^- charge 720
vicinal to C_{ipso} (Figure 8B, resonance path a), and because of 721
this, we assign an induced charge on C_{ipso} as $0.5\delta^+$ to illustrate 722
its magnitude as less than the induced δ^+ in **8** flanked by two 723
vicinal δ^- charges (cf. Figure 8A, route b). Another resonance 724
hybrid of **12** has a δ^- charge on C_{ipso} (Figure 8B, resonance 725
path b). Thus, the overall charge at C_{ipso} of **12** is represented 726
arbitrarily as $(\delta^- + 0.5\delta^+)$ (Figure 8B, **24**), while that of **8** is 727
represented as $(\delta^- + \delta^+)$ (Figure 8A, **23**). The greater δ^- 728
charge on C_{ipso} of **12** than on **8** likely conflicts with the δ^- 729
formed on C_β during the transition state of the deprotonation 730

731 step. Thus, this effect likely slowed the PaPAM reaction more
732 when **12** was used as substrate than when **8** was used.

733 It was interesting that the 2-furylalanine (**7**, 0.236 s⁻¹) was
734 turned over by PaPAM ~9-fold faster than the analogous 2-
735 thienylalanine (**12**, 0.026 s⁻¹), particularly since these two
736 heteroaromatic substrates have similar resonance hybrids
737 (Figure 8B). However, the more electronegative oxygen
738 compared to sulfur of **12** likely induced a larger δ^+ charge on
739 the vicinal C_{ipso} of **7**. Moreover, the more electronegative
740 oxygen of **7** distributes its lone pair electrons less than sulfur
741 and thus likely reduced the magnitude of the negative charge
742 (δ^-) in the canonical structures at C_{ipso} (Figure 8B, route b). A
743 smaller magnitude negative charge (arbitrarily set at 0.5 δ^-) at
744 C_{ipso} was assigned for **7** along with a larger induced positive
745 charge (assigned as "0.75 δ^+ " due to the more electronegative O
746 atom and adjacent δ^-) (see **25**), compared to the charges in **12**
747 (see **24**). The relative magnitude of the δ^+ on C_{ipso} is deemed
748 larger for **7** and thus was viewed to promote the removal of the
749 H _{β} in the PaPAM reaction. In addition, the higher proportion
750 of (2-furyl)acrylate (65.2%) from **7** (compared to only 9.1% (2-
751 thienyl)acrylate from **12**) suggests that the amination step
752 during the conversion of **7** to β -**7** is negatively affected by its
753 comparatively larger δ^+ on C_{ipso}.

754 **Comparing the Effects of Regioisomeric Substituents**
755 **on PaPAM Catalysis and Substrate Affinity.** The kinetic
756 parameters of the *meta/para/ortho*-regioisomers (bromo-**2/15/**
757 **20**; fluoro-**3/5/10**; chloro-**4/14/21**; nitro-**9/17/22**; methoxy-
758 **11/18/19**; and methyl-**13/16/6**) were compared. The binding
759 affinities (estimated by K_M) for the fluoro- and methyl-substrate
760 trifecta were approximately of the same order. However, the K_M
761 of PaPAM for the *o*-methoxy substrate **19** was nearly 10-times
762 smaller than for its *meta*- and *para*-isomers (Table 1). The K_T
763 values (μ M) for *o*-bromo- (**20**), *o*-chloro- (**21**), and *o*-nitro-
764 (**21**) substrates were 25-times smaller than the K_M values of
765 PaPAM for the corresponding *meta*- and *para*-isomers. This
766 supported the hypothesis that the *ortho*-substituted substrates
767 generally bound PaPAM better than the *meta*- and *para*-
768 isomers.

769 The relative binding affinity of each substrate was assessed as
770 a function of the six substituents (of varying electronic and
771 steric effects) in the *ortho*-, *meta*-, or *para*-position. The relative
772 binding affinities predicted from the calculated energies of
773 protein–ligand interactions and the internal energy of the
774 ligand [$E_{(p-l)} + E_{(l)}$] in the absence of energy minimization
775 matched the trend ($m \sim p > o$) in the experimental K_M values
776 for substrate isomers with halogens or nitro substituents
777 (Tables S1 and S2 of Supporting Information). This supports
778 the predictive value of the model in which the binding site
779 residues and substrate maintain the positions found in the
780 crystal structure with α -phenylalanine. The calculated vdW
781 interaction energies ($E_{V(p-l)}$) also follow the " $m \sim p > o$ " trend,
782 except for chloro compounds, which bound less tightly to
783 PaPAM (i.e., had higher K_M) than predicted by the $E_{V(p-l)}$ for
784 chloro series compared to other halogenated substrates (Tables
785 S1 and S2 of Supporting Information). The chloro series will be
786 discussed further in the Activity Cliff Analysis section below.

787 Importantly, the binding affinity order for all substrates
788 approximately corresponded to the vdW radii of the
789 substituents. PaPAM bound substrates with a fluoro group
790 (~1.5 Å) the best, followed by methyl (~1.9 Å), then bromo
791 and chloro groups (~1.8 Å). The least favorable substrate for
792 binding to PaPAM contained the bulkiest substituents: nitro
793 (~3.1 Å; from the vdW radii of the C_{ar}–N bond length and the

terminal O–N=O) and methoxy (~3.4 Å; from the vdW radii 794
of the C_{ar}–O bond and the methyl C–H bonds of the 795
methoxy).^{34,35} In general, PaPAM was predicted by $E_{V(p-l)}$ to 796
disfavor binding substrates with bulky groups at the *ortho*- 797
position, which correlated well with the experimental K_M 798
values. Surprisingly, substrates with *o*-methyl (**6**) (K_M = 88 799
 μ M) and *o*-methoxy (**19**) (K_M = 164 μ M) groups bound 800
PaPAM better than expected from their calculated $E_{V(p-l)}$ (55 801
and 108 kcal/mol, respectively) (Tables S1 and S2 of 802
Supporting Information). Binding of the *o*-methoxy group 803
could become more energetically favorable if it rotated slightly 804
from its crystallographic position to form hydrogen bonds with 805
Tyr320 in PaPAM (Figure S3 of Supporting Information). 806

Only three of the six *ortho*-isomers tested (fluoro, methoxy, 807
and methyl) were productive. The $k_{\text{cat}}^{\text{total}}$ of PaPAM for the *m*- 808
fluoro isomer (**3**, 0.031 s⁻¹) was only slightly greater than those 809
for the *p*-fluoro (**5**, 0.023 s⁻¹) and *o*-fluoro (**10**, 0.022 s⁻¹) 810
isomers (i.e., *meta*- \gtrsim *para*- \approx *ortho*-fluoro). The similar k_{cat} 811
values among the fluoro regioisomers suggested that the rate of 812
the PaPAM-catalyzed isomerization is indifferent to the 813
position of the fluoro group on the aryl ring. The turnover of 814
the *m*-methoxy isomer (**11**, 0.203 s⁻¹) was 10-times faster than 815
that for the *p*-methoxy isomer (**18**, 0.022 s⁻¹) and nearly 100- 816
times faster than that for the *o*-methoxy substrate **19** (0.003 817
s⁻¹) (i.e., *meta*- \gg *para*- $>$ *ortho*-methoxy). As discussed 818
previously, the *m*-methoxy of **11** is a "push–pull" substituent 819
that releases and withdraws electron density with the aryl ring 820
but is partially electron-withdrawing because of the electro- 821
negative oxygen atom. The balanced electronic effects were 822
proposed to speed-up the hydroamination step (Figure 6C) yet 823
not greatly retard the elimination step (Figure 6D). By contrast, 824
the same substituent at the *para*- and *ortho*-positions places a δ^- 825
charge directly on C_{ipso} connected to C _{β} and is therefore 826
imagined to significantly slow the elimination step for the *para/* 827
ortho-pair **18/19** (see Figure 6G or H). 828

The data show that PaPAM generally catalyzed the *meta*- 829
faster than the *para*- and *ortho*-substituted substrates containing 830
electron-donating substituents. The only exception was the *o*- 831
methyl regioisomer **6** (0.064 s⁻¹), which was turned over 832
slightly better than the *m*-methyl isomer (**13**, 0.058 s⁻¹) and 833
was ~4-fold better than the *p*-methyl isomer (**16**, 0.013 s⁻¹) 834
(i.e., *ortho*- \gtrsim *meta*- $>$ *para*-methyl). It is unclear why the trend 835
for the regioisomers of methylphenylalanine was an outlier 836
among the other regioisomeric series. Perhaps some as yet 837
unknown effect of the nonpolar *o*-methyl interacts with the 838
PaPAM active site better than the more polar *o*-methoxy- and 839
o-fluoro-counterparts. 840

In addition, the $k_{\text{cat}}^{\text{total}}$ values of PaPAM for the *meta*-substrates 841
of the *meta/para*-pairs (bromo-**2/15** and chloro-**4/14**) are 842
about 10-times greater than those for the corresponding *p*- 843
isomers. Similarly, the rate difference for the nitro-**9/17** *meta/* 844
para-pair was approximately 4-fold, favoring the *meta*- 845
substituted substrate (Table 1). As described earlier, the 846
"push–pull" of the electron pairs and the electronegativity of 847
chloro and bromo groups likely reduces their electron- 848
withdrawing magnitude compared to that of the strongly 849
electron-withdrawing nitro group. Thus, these electron-with- 850
drawing substituents at the *meta*- or *para*-position place a δ^+ on 851
C_{ipso} or inductively withdraw electron density from C_{ipso} 852
respectively. This δ^+ charge distribution likely facilitates the 853
elimination step (see Figure 6A and E) but likely impedes the 854
hydroamination steps (see Figure 6B and F), with the nitro 855
group doing so more strongly. 856

857 **Product Distribution.** The product pool catalyzed by
 858 PaPAM for 11 of the 19 productive substrates comprised the
 859 aryl acrylate at <10% and the β -amino acid at >90%. As
 860 discussed earlier, PaPAM converted **5** to an elevated proportion
 861 of *p*-fluorocinnamate (14.3%) over the amount of cinnamate
 862 byproduct made (at 7.2%) from the natural substrate **1**.
 863 Similarly, PaPAM catalyzed a larger proportion of the
 864 cinnamate analogues from the *ortho*-isomers **6** (16.4% *o*-
 865 methylcinnamate) and **19** (30% *o*-methoxycinnamate), *para*-
 866 isomers **16** (36.4% *p*-methylcinnamate) and **17** (52.0% *p*-
 867 nitrocinnamate), *meta*-isomers **3** (14.8% *m*-fluorocinnamate)
 868 and **13** (21.7% *m*-methylcinnamate), and the heteroaromatic
 869 compound **7** (65.2% (2-furyl)acrylate). As described earlier, we
 870 propose for these substrates that the amination rate was
 871 decreased by the electronic effects of the functional group.

872 **Relationship between PaPAM-Substrate Interaction**
 873 **Energies, Flexibility, and K_M .** The calculated interaction
 874 energies obtained from modeling provided insight into which
 875 energy terms correlated best with the K_M values of PaPAM for
 876 each substrate. They also helped elucidate which substrate-
 877 docking model correlated best with experimental K_M . The static
 878 model placed the substrates identical to the trajectory of α -
 879 phenylalanine in the crystal structure. The flexible model,
 880 however, allowed bond-rotational motion for the protein side
 881 chains to relieve unfavorable interactions. The static modeling
 882 showed that the experimental K_M for each substrate (except for
 883 three unreactive *o*-bromo, *o*-chloro, and *o*-nitro substrates **20**–
 884 **22**) increased with total energy [$E_{(p-l)} + E_{(l)}$], which
 885 approximated $\Delta G_{\text{binding}}$ and reflected unfavorable interactions
 886 (Figure 10). The linear correlation coefficient (*ccoef*) between
 887 [$E_{(p-l)} + E_{(l)}$] and K_M was 0.48 (Figure 10), while the *ccoef*
 888 between $E_{V(p-l)}$ and K_M was 0.54 (Figure S4 of the Supporting
 889 Information). Incidentally, the *ccoef* between the Coulombic
 890 energy [$E_{C(p-l)}$], a component of $E_{(p-l)}$, and K_M was lower (0.33;
 891 Figure S5 of the Supporting Information). These results
 892 suggested that the steric effects in the protein–ligand adduct
 893 and within the ligand are dominant over electrostatic
 894 interactions upon substrate binding. Moreover, when energy
 895 minimization was used to relieve vdW overlap between each
 896 substrate and the active site residues of PaPAM (see Figure S4
 897 of the Supporting Information), the *ccoef* between [$E_{(p-l)} + E_{(l)}$]
 898 and K_M decreased from 0.48 to 0.35. This result emphasizes the
 899 importance of vdW overlap-induced strain in affecting the
 900 binding affinity of PaPAM for its substrates.

901 Another reason why energy minimization of the protein–
 902 ligand interaction likely affected the correlation between [$E_{(p-l)}$
 903 + $E_{(l)}$] and K_M is that, in some cases, groups were rotated that
 904 should have remained rigid. This may be due to inaccuracies in
 905 energy-minimization force field parameters for some functional
 906 groups, due to the prodigious challenge in deriving correct
 907 torsional energy barrier profiles for all bonds between all types
 908 of functional groups that occur in organic molecules. For
 909 instance, the nitro substituent was rotated out-of-plane relative
 910 to the phenyl ring during energy minimization. However, our
 911 analysis of 200 nitrophenyl groups in small-molecule crystal
 912 structures in the Cambridge Structural Database 1.1.1 ([http://](http://www.ccdc.cam.ac.uk)
 913 www.ccdc.cam.ac.uk) indicated that 87.5% of the nitrophenyl
 914 groups are entirely coplanar, regardless of other features in the
 915 structure.³⁶ The energy minimization-free protocol provided
 916 intermolecular energy values that correlated better with K_M .
 917 This observation suggests that the crystallographic placement of
 918 the substrates and PaPAM was ideal for most substrates and

that modeling alternative, energy-minimized side group 919
 positions may reflect catalytically unproductive conformations. 920

Substrates were identified as either in the NH_2 -*cis* or NH_2 - 921
trans configuration (Figure 9) if the difference (ΔE_{tot}) in the 922 9

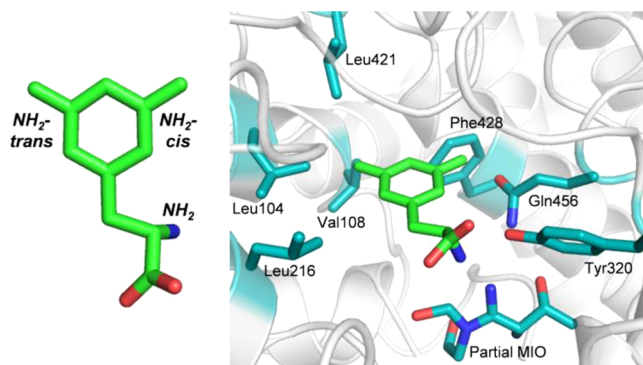


Figure 9. Overlay of the NH_2 -*cis* and NH_2 -*trans* configurations is illustrated, using the *m*-methyl-(*S*)- α -phenylalanine substrate (atoms are C, green; N, blue; and O, red). The methyl group can be positioned on the same side (NH_2 -*cis*) or the opposite side (NH_2 -*trans*) as the reactive amino group of the chiral substrate (left). An overlay of the NH_2 -*cis* and NH_2 -*trans* active configurations of *m*-methyl-(*S*)- α -phenylalanine is modeled in the crystallographic position of α -phenylalanine in PaPAM (PDB ID 3UNV). A partial MIO and the active site residues that cause van der Waals overlap with the ligands are shown (C, light blue; N, dark blue; and O, red). SLIDE and other docking tools cannot model covalently bound ligands, which are interpreted as disallowed steric overlap (right). Thus, the alkene carbon atoms of the MIO (cf. Figure 2) were removed to dock the substrate.

[$E_{(p-l)} + E_{(l)}$] term for models of the two orientations was >25 923
 kcal/mol (Tables S3, Supporting Information). Using this limit, 924
o-methoxy- (**19**), *m*-methyl (**13**), *m*-bromo- (**2**), *m*-nitro- (**9**), 925
 and *m*-chloro- (**4**) substrates were predicted to conform to the 926
 NH_2 -*cis* configuration, while *p*-methoxy- (**18**), *o*-methyl- (**6**), *o*- 927
 chloro- (**21**), *o*-bromo- (**20**), and *o*-nitro- (**22**) substrates were 928
 predicted to favor the NH_2 -*trans* configuration (Figure 10 and 929 f10
 Table S3, Supporting Information). In substrate **18**, the methyl 930
 of the methoxy group was predicted to adopt a quasi NH_2 -*cis* 931
 configuration. 932

For *meta*-substituted substrates, the NH_2 -*cis* is the preferred 933
 configuration because Leu104, Val108, and Leu421 sterically 934
 hinder the NH_2 -*trans* conformers more than Gln456, Phe428, 935
 Gly85, Phe455, and Tyr320 hinder the NH_2 -*cis* conformers 936
 (Figure 9). However, *m*-methoxy substrate **18** has no 937
 preference for the NH_2 -*cis* or NH_2 -*trans* configuration, as 938
 energy calculations suggest that the methoxy group interacts 939
 similarly with active sites residues on either side. It should be 940
 noted that Phe428, Val108, and Leu421 also sterically hinder 941
 substrates with *para*-substituted substrates. The *ortho*-substi- 942
 tuted substrates (except for the *o*-methoxy substrate **19**) are 943
 energetically more likely to adopt the NH_2 -*trans* configuration. 944
 The *ortho*-substituted substrates have steric barriers created by 945
 residues Phe428, Gln456, and Tyr320 on the NH_2 -*cis* side of 946
 PaPAM (Figure 9). In addition, the NH_2 -*trans* conformers of 947
 the *ortho*-substituted substrates encounter lower $E_{V(p-l)}$ between 948
 Leu216 and Leu104 than between Tyr320 and Gln456 of the 949
 NH_2 -*cis* conformers (Figure 9). As mentioned previously, the *o*- 950
 methoxy substrate **19** bound to PaPAM better than expected 951
 from its calculated vdW energy ($E_{V(p-l)}$) (Tables S1 and S2, 952
 Supporting Information). The energy calculations predict that 953

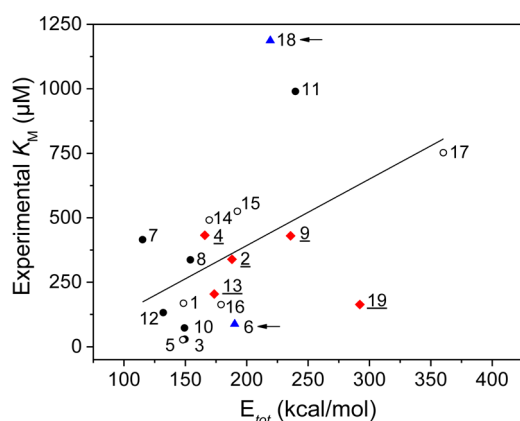


Figure 10. Plot of experimental K_M and $E_{tot} = E_{(p-l)} + E_{(l)}$ (protein–ligand interaction energy) + $E_{(l)}$ (the intraligand energy) calculated with Szybki. The substrates were modeled statically, according to the trajectory of α -phenylalanine in the PaPAM crystal structure, without energy minimization. Substrates are labeled according to Table 1, and the lower energy of the two configurations [NH_2 -cis (red \blacklozenge , underlined) and or NH_2 -trans (blue \blacktriangle , with arrows)] is plotted for the substrates. Substrates with no significant difference in energy between the NH_2 -cis and NH_2 -trans ($\Delta E < 25$ kcal/mol) are shown as filled circles (\bullet). Substrates with *para*-substituents (except *p*-methoxy) without an NH_2 -cis or NH_2 -trans preference are shown as open-circles (\circ). Nonproductive substrates 20–22 (not shown) were predicted to prefer the NH_2 -trans orientation in the PaPAM active site.

19 favors the NH_2 -cis conformer. This orientation is consistent with the hypothesis that the *o*-methoxy of 19 is near Tyr320 of PaPAM and can potentially form an energetically favorable hydrogen bond. Of the nine substrates (1, 3, 5, 6, 10, 12, 13, 16, and 19) that bound PaPAM the best ($K_M \lesssim 200 \mu M$, i.e., not $>20\%$ over the K_M of PaPAM for 1), all except the *o*-methoxy substrate 19 ($E_{V(p-l)} = 108$ kcal/mol) had $E_{V(p-l)} \leq 55$ kcal/mol (designated as the energy threshold with low vdW overlap). However, the majority of the poorest binding substrates, with $K_M > 500 \mu M$, and nonproductive substrates had $E_{V(p-l)} \geq 80$ kcal/mol, with the *p*-nitro- (17), *o*-bromo- (20), and *o*-nitro- (22) substrates predicted to have comparatively higher vdW energy at ≥ 190 kcal/mol (Table S3, Supporting Information). Relative binding energy, based on $E_{V(p-l)}$, is thus highly predictive of PaPAM having a potentially high or low affinity for a substrate.

Generally, for productive substrates where the K_M of PaPAM was $\leq 500 \mu M$, the relative energy [$E_{(p-l)} + E_{(l)}$] of the NH_2 -cis and NH_2 -trans configurations tended to be ≤ 200 kcal/mol (see Table S3, Supporting Information). It was intriguing to find that substrates that bind PaPAM with the least affinity (highest K_M) (compound 18) or were nonproductive (21, 20, and 22) had differences of ≥ 150 kcal/mol between the two orientations (see Table S3, Supporting Information). These results suggest that either the substituent on the substrate causes the enzyme to preferentially bind the substrate in one orientation over the other or that low vdW barriers in the pocket enable the substrate to rotate to an active conformation for turnover.

The computational analyses identified residues that will help guide future mutational studies. Proposed mutations are envisioned to increase the binding affinity of PaPAM for various substrates. The K_M of PaPAM was higher for several substrates with *meta*- and *para*-substituents (except fluoro and methyl) than for 1. The presumed lower binding affinity was likely due to steric interactions between the substituents and

the active site residues of PaPAM. As mentioned herein, *meta*-substituted substrates were shown by modeling to prefer the NH_2 -cis configuration to avoid steric clashes with branched hydrophobic residues. Mutation of Leu104, Val108, and Leu421 to alanines may improve the binding of *meta*-substituted substrates by providing flexibility to bind in the NH_2 -cis or NH_2 -trans configuration. Further, computational models predicted that *para*-substituents sterically clash with Phe428, Val108, and Leu421. Therefore, exchange of these residues for alanine may facilitate the binding of *para*-substituted substrates. Surprisingly, the computational analysis predicted that all *ortho*-substituted α -arylalanines bound well to PaPAM; however, relief of the active site sterics may enable these *ortho*-substituted α -arylalanines to better access a catalytically competent conformation and improve the turnover number for these substrates. Some of the computationally predicted targets for mutation are supported, in part, by an earlier study on a related, MIO-dependent phenylalanine ammonia lyase. The earlier work showed that a Val83Ala mutation (positioned analogously to Val108 of PaPAM) in the substrate binding pocket resulted in enzyme catalytic efficiency at ~ 4 -fold greater than that of the wild-type enzyme. The efficiency enhancement of the mutant resulted from a ~ 5 -fold reduction in K_M and a ~ 20 -fold increase in k_{cat} compared to the parameters of the wild-type enzyme.³⁷

The flexible docking feature of SLIDE provided another approach to reduce vdW collisions between the crystallographic conformation of PaPAM side chains and substituents on the arylalanine substrates oriented in the NH_2 -cis and NH_2 -trans configurations. After application of the SLIDE flexibility modeling in the site, no significant correlation was found for SLIDE-calculated interaction energies and K_M values except for the unsatisfied polar interaction term: $E_{(p-l)}$ ($ccoeff = 0.13$), hydrophobic interaction energy, $E_{H(p-l)}$ ($ccoeff = -0.19$), and unfavorable energy of interaction due to unpaired or repulsive polar interactions, $E_{UP(p-l)}$ ($ccoeff = 0.44$). SLIDE also assessed the sum of unresolvable vdW overlaps in each complex, in \AA , following flexibility modeling. The correlation of this value with K_M , $ccoeff = 0.27$, was positive but somewhat lower than the correlation found between the Szybki intermolecular vdW energy and K_M in the absence of substrate or protein motion relative to the crystal structure ($ccoeff$ of 0.54). This is consistent with the decrease in correlation between Szybki intermolecular vdW energy and K_M (from 0.54 to 0.42) upon energy minimization, reflecting changes in the conformation of the complex. These results indicate that the favorability of vdW interactions and the absence of unsatisfied polar interactions when the substrate and protein are in their crystallographic conformation are the strongest predictors for favorable substrate K_M .

Activity Cliff Analysis. SALI values were used to identify “activity cliffs” that represent large changes in PaPAM binding affinity among structurally similar substrates.²² The most obvious activity cliffs were found for substrates with fluoro-, methyl-, and chloro-substituents at the same positions (Figure 11). The chloro- and methyl-groups share similar vdW radii. When chloro is attached to an aryl ring carbon, its electron density delocalizes through resonance, placing a partial positive charge at the pole of the chloro atom furthest from the ring carbon.³⁸ The polarizability of the halogen atoms increases with atomic orbital size; therefore, the trend to form a halogen bond is in the order fluoro $<$ chloro $<$ bromo $<$ iodo, where iodo normally forms the strongest interactions. Thus, the chloro-

- 1144 (15) Hawkins, P. C.; Nicholls, A. *J. Chem. Inf. Model.* **2012**, *52*,
1145 2919–2936.
- 1146 (16) Jakalian, A.; Jack, D. B.; Bayly, C. I. *J. Comput. Chem.* **2002**, *23*,
1147 1623–1641.
- 1148 (17) Nicholls, A.; Wlodek, S.; Grant, J. A. *J. Comput.-Aided Mol. Des.*
1149 **2010**, *24*, 293–306.
- 1150 (18) Wlodek, S.; Skillman, A. G.; Nicholls, A. *J. Chem. Theory*
1151 *Comput.* **2010**, *6*, 2140–2152.
- 1152 (19) Halgren, T. A. *J. Comput. Chem.* **1996**, *17*, 490–519.
- 1153 (20) Zavodszky, M. I.; Rohatgi, A.; Van Voorst, J. R.; Yan, H.; Kuhn,
1154 L. A. *J. Mol. Recognit.* **2009**, *22*, 280–292.
- 1155 (21) Zavodszky, M. I.; Sanschagrin, P. C.; Korde, R. S.; Kuhn, L. A. *J.*
1156 *Comput.-Aided Mol. Des.* **2002**, *16*, 883–902.
- 1157 (22) Guha, R.; Van Drie, J. H. *J. Chem. Inf. Model.* **2008**, *48*, 646–
1158 658.
- 1159 (23) Hawkins, P. C.; Skillman, A. G.; Nicholls, A. *J. Med. Chem.* **2007**,
1160 *50*, 74–82.
- 1161 (24) Mutatu, W.; Klettke, K. L.; Foster, C.; Walker, K. D.
1162 *Biochemistry* **2007**, *46*, 9785–9794.
- 1163 (25) Schuster, B.; Rétey, J. *Proc. Natl. Acad. Sci. U.S.A.* **1995**, *92*,
1164 8433–8437.
- 1165 (26) Wanninayake, U.; DePorre, Y.; Ondari, M.; Walker, K. D.
1166 *Biochemistry* **2011**, *50*, 10082–10090.
- 1167 (27) Weiner, B.; Szymanski, W.; Janssen, D. B.; Minnaard, A. J.;
1168 Feringa, B. L. *Chem. Soc. Rev.* **2010**, *39*, 1656–1691.
- 1169 (28) Szymanski, W.; Wu, B.; Weiner, B.; de Wildeman, S.; Feringa, B.
1170 L.; Janssen, D. B. *J. Org. Chem.* **2009**, *74*, 9152–9157.
- 1171 (29) Ratnayake, N. D.; Wanninayake, U.; Geiger, J. H.; Walker, K. D.
1172 *J. Am. Chem. Soc.* **2011**, *133*, 8531–8533.
- 1173 (30) Hammett, L. P. *J. Am. Chem. Soc.* **1937**, *59*, 96–103.
- 1174 (31) Hoffmann, J.; Klicnar, J.; Štěrba, V.; Večeřa, M. *Collect. Czech.*
1175 *Chem. Commun.* **1970**, *35*, 1387–1398.
- 1176 (32) Fernández, I.; Wu, J. I.; von Ragué Schleyer, P. *Org. Lett.* **2013**,
1177 *15*, 2990–2993.
- 1178 (33) Laing, M. *J. Chem. Educ.* **1987**, *64*, 124.
- 1179 (34) Batsanov, S. S. *Russ. Chem. Bull.* **1995**, *44*, 18–23.
- 1180 (35) Li, A. J.; Nussinov, R. *Proteins* **1998**, *32*, 111–127.
- 1181 (36) Carpy, A. J. M.; Haasbroek, P. P.; Ouhabi, J.; Oliver, D. W. *J.*
1182 *Mol. Struct.* **2000**, *520*, 191–198.
- 1183 (37) Xiang, L.; Moore, B. S. *J. Bacteriol.* **2005**, *187*, 4286–4289.
- 1184 (38) Metrangolo, P.; Meyer, F.; Pilati, T.; Resnati, G.; Terraneo, G.
1185 *Angew. Chem., Int. Ed.* **2008**, *47*, 6114–6127.